

Master thesis

Local and non-local relaxation dynamics of hot
electrons and holes analysed by time resolved linear
photoemission

Florian Kühne

Faculty of physics, University Duisburg-Essen, Lotharstrasse 1, D-47057
Duisburg, Deutschland

Faculty of chemistry, University Duisburg-Essen, Universitätsstr.5,
D-45141 Essen, Deutschland
21.08.2020

Abstract

This thesis utilised a time resolved linear photoemission (*tr*-LPE) measurement technique with a femtosecond resolution in a pump-probe scheme to analyse the transport mechanisms of laser excited non-equilibrium dynamics in a gold (Au) / iron (Fe) epitaxial heterostructure system. The motivation of the work was to observe ballistic propagation in Au / Fe layered systems. Previous efforts have shown, that the relaxation times increased with lower energies due to a bigger phase space. The concept is that at low enough energies for thin films the phase space would become large enough to observe ballistic propagation. The material system Au / Fe / MgO(001) was chosen, because of the epitaxial growth and the pristine interface conditions, as shown by Alekhin et al. [2] and Razdolski et al. [35]. Here Au is being probed as the propagation layer, where the transport occurs. And Fe acts as an excited electron injector layer, because of the good absorption, in the back side pump / front side probe and due to the shorter mean free path in Fe than in Au, as a sink for the excited electrons in case of front side pump / front side probe. The described dynamics are going to be studied by varying the thickness of the Au-layer. To differentiate the separate transport and relaxation contributions a previously developed back side pump / front side probe was used along with the usual front side pump / front side probe. The work of Beyazit et al. utilised *tr*-2PPE giving good insight into the non-equilibrium dynamics, but with limited access to electrons close to Fermi-level (E_F). The novelty of this work is that with *tr*-LPE the region from the Fermi-level to the pump photon energy can be probed above E_F , giving complementary data to previous experiments [9]. This is as well proof of work for the *tr*-LPE setup in back side pump configuration. Besides the extensively studied excited electron states, *tr*-LPE allows the observation of hole states below the Fermi-level and their relaxation back into thermal equilibrium through recombination. This work will try to further consolidate our understanding on how electron and hole relaxation dynamics interact and compete with the transport into the heterostructure. By analysis of the LPE signal as a function of pump-probe time delay an energy dependence for the peak intensity delay, like in Beyazit et al. [9], could be shown. In case of back side pump the analysis of electrons showed the same behaviour with lower energy electrons arriving later at the detector than the electrons with higher energy. This effect is thickness dependent indicating transport processes. Because the 'hot' electron dynamics around the Fermi-level are measured secondary electron dynamics are observed repopulating lower excited states and competing with the relaxation dynamic. Front side pump showed no delay in peak intensity, because the electrons did not have to propagate through the Au-layer. Laser calculations done in this work, show that for back side pump the excitation is predominantly in Fe with negligible excitation in Au, while in front side pump the Au-layer is homogeneously excited creating a gradient free non-equilibrium electron distribution. By determining

the energy density it was demonstrated that in back side pump more energy density reaches the Au surface with thinner gold layers, dissipating less incident energy during propagation, while in front side pump the energy density decreases with decreasing film thickness. Combination of the calculated incident laser absorption with the measured energy densities after propagation show, that in front side pump a bigger proportion of the actually absorbed energy reaches the detector compared to back side pump. For back side pump the efficiency of injection decreases with increasing film thickness. This loss of energy density is attributed to scattering events during propagation through the Au-layer. Through careful analysis of the energy resolved transients a spectral feature close to the Fermi-level, exclusive to back pump, could be identified. This peak is ascribed to d-band electrons in Fe. This work could measure depleted ground states as well as excited electrons, these electron holes below the Fermi-level exhibit a similar relaxation dynamic to the excited states, decaying on a timescale of 500 fs.

Lokale und nicht lokale Relaxationsdynamiken von angeregten Elektronen und Löchern analysiert durch zeitaufgelöste lineare Photoemission

Zusammenfassung

In dieser Arbeit wird das zeitaufgelöste lineare Photoemissionsmessverfahren (*tr*-LPE) mit einer femtosekunden Auflösung in einem Pump/Probe-Schema verwendet um die Transportmechanismen von Laser angeregten nicht-gleichgewichts Dynamiken in einem Au / Fe epitaktischen Heterosystem zu analysieren. Das Materialsystem Au / Fe / MgO(001) wurde ausgesucht, wegen dem epitaktischen Wachstum und makellosen Grenzflächen, wie es in den Arbeiten von Alekhin et al.[2] und Razdolski et al.[35] gezeigt wurde. Au agiert in den Experimenten mit rückseitiger Anregung als Propagationsschicht und Eisen agiert als ein Injektor für angeregte Elektronen, weil es gute Absorptionseigenschaften hat, hingegen im Fall der vorderseitigen Anregung hat Eisen die Funktion einer Senke für die angeregten Elektronen, da die mittlere freie Weglänge um einiges kürzer ist als in Au. Die beschriebenen Dynamiken werden untersucht indem die Dicke der Goldschicht variiert wird. Um die Anteile von Transport- und Relaxationsdynamiken zu entschlüsseln wird eine zuvor entwickelte rückseitigen Anregung / vorderseitigen Abfrage neben der etablierten vorderseitigen Anregung / vorderseitigen Abfrage verwendet. Durch die Analyse der Relaxationszeiten kann eine Abhängigkeit von der Schichtdicke bestätigt werden, wie es in Beyazit et al.[9] bereits gezeigt wurde. Die Arbeit von Beyazit et al. nutzt *tr*-2PPE, welche einen guten Einblick in die nicht-Gleichgewichtsdynamik gibt, aber mit limitiertem Zugang auf Elektronen nahe der Fermi-Kante. Die Neuheit in dieser Arbeit ist, dass mit *tr*-LPE die Region vom Fermi-level bis 1.55 eV über der Fermi-Kante untersucht werden kann, was komplementäre Daten zu den vorherigen Experimenten liefert [9]. Weiterhin ist diese Arbeit ein Beweis für die Ausführbarkeit von *tr*-LPE Aufbau mit rückseitiger Anregung. Neben den umfangreich studierten angeregten Zuständen von Elektronen, erlaubt *tr*-LPE die Beobachtung von Lochzuständen unterhalb der Fermi-Kante und ihre Relaxation durch rekombination. Diese Arbeit wird versuchen unser Verständnis von Elektronen- und Lochrelaxationsdynamiken und das Wissen über das Zusammenspiel dieser Dynamiken mit dem Transport in das Heterosystem zu vertiefen.

Acknowledgements

Contents

Abstract	I
Zusammenfassung	IV
List of Figures	XI
List of Tables	XI
Acronyms	XII
1 Introduction	1
2 Theoretical Background	2
2.1 Elementary Scattering Processes	2
2.1.1 Electron-Electron Interactions	3
2.1.2 Electron-Phonon Interactions	3
2.2 Electron Transport	4
2.3 Time Resolved Linear Photoemission Spectroscopy	5
2.4 Optical Penetration Depth	7
2.5 Hole Dynamics	8
2.6 Au/Fe/MgO(001) Heterostructure System & Electronic Bandstructure	8
2.6.1 Chemical Properties of Gold	9
2.6.2 Chemical Properties of Iron	11
3 Experimental Methods	13
3.1 Vacuum Chamber	13
3.1.1 Magazine and Load-lock	13
3.1.2 Upper Chamber	13
3.1.3 Lower Chamber	15
3.2 Laser Setup	16
3.2.1 Alignment	17
3.3 Determination of Spatial and Temporal Overlap using Thin Lead Films on Si(001)	17
3.4 Experimental Configuration	19
3.5 Determining the Electronic Start Signal	20
3.6 Setting the Relative Time Delay	21
4 Analysis	23
4.1 Calculation of Laser Absorption Profile	23
4.2 Estimation of the Energy Density by the Fermi-Level	28
4.3 Determining the width of the Fermi-distribution function	29
4.4 Fermi-Level Fit and Normalisation	30
4.5 Background Subtraction	33
4.6 Relative Number of Electrons and Holes	35
4.7 Calculation of the Energy Density in the System	39
4.8 Energy Density	40
4.8.1 Relaxation times	43
4.9 Signal to Noise Ratio	46

4.10	Analysis of the Time Independent Energy Transients	47
5	Discussion	50
5.1	Energy resolved transients	50
5.2	Relaxation times	50
6	Outlook	52
7	References	53

List of Figures

1	The characteristical timescales of electron dynamics in metals [7]. . . .	2
2	Depiction of the DOS against the energy of the electronic system (left) and the velocity dispersion of the hot electrons away from the surface in the z direction (right). (a) describes the non-equilibrium electrons at time zero during excitation, (b) is in the timescale of thermal equilibrium for the electrons and (c) describes thermal and lattice equilibrium [20].	4
3	Anomalous diffusion coefficient for a period of time of a couple of picoseconds. Here an anomalous diffusion coefficient of one expresses a ballistic motion, while two characterises a diffusive motion [6].	5
4	Depiction of the tr -two-photonphotoemission (2PPE) (left) and LPE (right) excitation process for the model system using the workfunction Φ_{Au} of Au. Hatched area is the detected energy window above E_F . . .	6
5	Illustration of optical penetration for thin film samples, in front side pump [25].	7
6	Layout of the sample film thicknesses (left) and three-dimensional visualisation (right). The lateral dimensions of the sample are 9 mm by 9 mm.	8
7	The refractive index n of gold from 200 to 2000 nm. Taken out of the optical handbook from Palik [32].	9
8	The extinction coefficient κ of gold from 200 to 2000 nm. Taken out of the optical handbook from Palik [32].	9
9	Calculated band structure of gold, the dashed line corresponds to the Fermi-level. Taken from Papaconstantopoulos [33].	10
10	The density of states of gold taken from Papaconstantopoulos [33]. The dashed line depicts the Fermi-level.	11
11	The refractive index n of iron from 200 to 2000 nm. Taken from Johnsen and Christy [22].	11
12	The extinction coefficient κ of iron from 200 to 2000 nm. Taken from Johnsen and Christy [22].	11
13	Density of states of bcc-iron split into majority (spin up) and minority (spin down) electrons. Taken from Alekhin [1].	12
14	Constructional drawing of the magazine and load-lock [10].	13
15	Schematic illustration for the upper chamber [10]. The different components of the chamber are explained in the text by the indexed numbers.	14
16	Schematic illustration of the lower chamber [10].	15
17	A schematic view of the femtosecond laser setup.	16
18	Sketch of the alignment beam path for front side pump taken from the PhD thesis of A. Seyd [38].	17
19	CCD-camera recording of the 1.55 eV pump beam in the focus point with a diameter of 212 μm vertically and 180 μm horizontally at FWHM. The black scale is 112 μm large and the colorscale depicts the pixel intensity.	18
20	CCD-camera recording of the 6 eV probe beam in the focus point with a diameter of 168 μm vertically and 156.8 μm horizontally at FWHM. The black scale is 112 μm large and the colorscale depicts the pixel intensity.	18

21	Photoemission spectrum of a thin lead film on Si(001). The black line depicts the 6 eV Probe spectrum and the red line the correlated signal.	19
22	Photoemission spectrum of only the pump pulse, same scales as Fig. 21 for comparison.	19
23	Experimental sample setup as used in this thesis.	20
24	Energy diagram of the sample and detector with a negative bias voltage U_B	20
25	Pump-probe spectra after loading it with the provided Igor file. The colorcode goes from blue (low intensity) over brown to white (high intensity) indicating the measured photoelectron yield.	22
26	Blue: The electrons with the highest kinetic energy around time zero (integrated over 100 meV). They are found at a kinetic energy of 3.85 eV and red: the Gaussian fit to model the position of time zero. Fitting parameters can be found in the text.	23
27	Laser absorption profile for the 800 nm on the back side of 30 nm Au / 7 nm Fe. With the black trace as the intensity of the electric field of the light, the blue the absorbed laser power $P(z)$ normalised to one at the end of the sample and the red trace showing the differential of the absorbed laser power $P(z)$	25
28	Laser absorption profile for the 200 nm probe beam on the surface of 5 nm Au / 7 nm Fe. With the black trace as the intensity of the electric field of the light, the blue the absorbed laser power $P(z)$ normalised to one at the end of the sample and the red trace showing the differential of the absorbed laser power $P(z)$	26
29	Laser absorption profile for the 800 nm pump beam on the surface of 5 nm Au / 7 nm Fe / Magnesium oxide (MgO) in front side pump configuration.	27
30	Time resolved spectrum at 200 fs before excitation for 5 nm Au / 7 nm Fe / MgO in back side pump / front side probe configuration. The blue line is the experimental data and the red line the fitted Fermi-function. Fitting parameters can be found in the text.	28
31	Time resolved spectrum at time zero for 5 nm Au / 7 nm Fe / MgO in back side pump / front side probe configuration. The blue line is the experimental data and the red line the fitted Fermi-function. Fitting parameters can be found in the text.	28
32	Several calculated Fermi-Dirac distributions for different temperatures. The blue line is a guide to the eye indicating the tangent used for the width determination of the 300 K trace.	30
33	Linear representation of the normalised correlated signal of 5 nm Au, 7 nm Fe using the front side pump configuration.	31
34	Linear representation of the normalised correlated signal of all samples.	32
35	Linear plot between -0.6 eV and 0.6 eV around the Fermi-level for 15 nm Au in back side pump geometry. Data points (blue) and fit (red). Fit parameters can be found in the text.	32
36	Linear plot of the Fermi-edge fit for 15 nm Au in back side pump geometry. Data points (blue) and fit (red). Fit parameters can be found in the text.	32

37	Linear plot of the Fermi-edge fit for 30 nm Au in front side pump geometry. Data points (blue) and fit (red). Fit parameters can be found in the text.	33
38	Time and energy resolved LPE spectrum for 5 nm Au / 7 nm Fe / MgO in back side pump configuration. The red rectangle indicates the energy dependent transient used for background subtraction.	34
39	2D plot of the background subtracted spectrum for 5 nm Au / 7 nm Fe / MgO in back side pump configuration. Red intensity is above zero, while blue is below.	35
40	Energy dependent spectrum at time zero.	36
41	Energy dependent spectrum of time zero. Summed up in 100 meV bins for computational reasons.	36
42	Electrons and holes for 5 nm Au / 7 nm Fe / MgO in back side pump configuration. Black and blue: Electrons, gold and red: Hole states. . .	37
43	relative number of electrons and holes for 5 nm Au / 7 nm Fe / MgO in back side pump configuration. Black: Electrons, Red: Hole states . . .	38
44	relative number of electrons and holes for 5 nm Au / 7 nm Fe / MgO in front side pump configuration. Black: Electrons, Red: Hole states, Green: Fermi-level.	38
45	Energy density plot over the entire measurement time of 5 nm Au in back side pump configuration, different colours describe different integral bounds.	40
46	Energy integrated, time dependent transients from E_F to 1.7 eV for 5 nm Au, 7 nm Fe using the front side pump / front side probe configuration.	41
47	Energy integrated, time dependent transients from E_F to 1.7 eV for 5 nm Au, 7 nm Fe using the back side pump / front side probe configuration.	41
48	Energy integrated, time dependent transients from E_F to 1.7 eV for 15 nm Au, 7 nm Fe using the front side pump / front side probe configuration.	42
49	Energy integrated, time dependent transients from E_F to 1.7 eV for 15 nm Au, 7 nm Fe using the back side pump / front side probe configuration.	42
50	Energy integrated, time dependent transients from E_F to 1.7 eV for 30 nm Au, 7 nm Fe using the front side pump / front side probe configuration.	42
51	Energy integrated, time dependent transients from E_F to 1.7 eV for 30 nm Au, 7 nm Fe using the back side pump / front side probe configuration.	42
52	Energy integrated, time dependent transients from E_F to 1.7 eV for 5 nm Au, 7 nm Iron using the front side pump / front side probe configuration normalised to -0.1 eV.	44
53	Energy integrated, time dependent transients from E_F to 1.7 eV for 5 nm Au, 7 nm Iron using the back side pump / front side probe configuration normalised to -0.1 eV.	44
54	Energy integrated, time dependent transients from E_F to 1.7 eV for 15 nm Au, 7 nm Iron using the front side pump / front side probe configuration normalised to -0.1 eV.	44

55	Energy integrated, time dependent transients from E_F to 1.7 eV for 15 nm Au, 7 nm Iron using the back side pump / front side probe configuration normalised to -0.1 eV.	44
56	Energy integrated, time dependent transients from E_F to 1.7 eV for 30 nm Au, 7 nm Iron using the front side pump / front side probe configuration normalised to -0.1 eV.	45
57	Energy integrated, time dependent transients from E_F to 1.7 eV for 30 nm Au, 7 nm Iron using the back side pump / front side probe configuration normalised to -0.1 eV.	45
58	Energy integrated, time dependent transients from E_F to 1.7 eV for 5 nm Au, 7 nm Iron using the front side pump / front side probe configuration normalised to -0.1 eV. Focused around time zero.	45
59	Energy integrated, time dependent transients from E_F to 1.7 eV for 5 nm Au, 7 nm Iron using the back side pump / front side probe configuration normalised to -0.1 eV. Focused around time zero.	45
60	5 nm Au / 7 nm Fe in front side pump / front side probe geometry. . . .	47
61	30 nm Au in back side pump configuration.	47
62	Energy transients of 5 nm Au / 7 nm Fe in back side pump configuration for different times. Timesteps Δt between data points are 60 fs.	48
63	Energy transients of 5 nm Au / 7 nm Fe in back side pump configuration for different times with emphasis on below the Fermi-level. Timesteps Δt between data points are 60 fs.	48
64	Energy transients of 5 nm Au / 7 nm Fe in back side pump configuration with emphasis on a spectral feature slightly above the Fermi-level for different times. Timesteps Δt between data points are 60 fs.	49

List of Tables

1	Optical penetration depth λ_{OPD} for the different constituents and wavelengths.	7
2	X-ray OPTics utilities (X-op) inputs FP means front side pump, BP means back side pump	24
3	Estimated λ_{OPD} in nm for the 1.55 eV beam. FP meaning frontside pump and BP back side pump.	26
4	Absorbed fluence of the 1.55 eV for the different constituents, all values are given in $\mu\text{J}/\text{cm}^2$	27
5	Energy density at time zero	43
6	Injection efficiency	43
7	Relaxation times	46
8	Signal to Noise ratio	46

Acronyms

E_F Fermi-level. I, VIII, 2, 3, 5, 6, 10, 21, 23, 29–33, 35, 37, 39–41, 46–51

t_0 time zero. 22, 45

β -BBO low temperature β phase barium borate. 16, 18

- tr-LPE** *time-resolved* linear Photoemission. 1, 6, 17, 18, 33, 37, 50–52
- 2PPE** *tr*-two-photonphotoemission. VIII, 5, 6
- Au** gold. I, II, IV, VIII–XI, 1, 3, 5–9, 12, 19, 22–29, 31–35, 37–52
- bbc** body-centered cubic. 11
- BP** back side pump. 1, 15, 16, 24–26, 46–49
- CCD** Charge-coupled device. 17, 18, 27
- DOS** density of states. 10, 11, 29
- e-e scattering** electron-electron scattering. 2–4
- e-ph scattering** electron-phonon scattering. 4, 5
- eTOF** electron time of flight spectrometer. 15, 20
- Fe** iron. I, II, IX–XI, 1, 3, 5, 7–9, 11, 12, 19, 22–28, 31, 34, 35, 37, 38, 41, 42, 45–52
- FP** front side pump. 1, 15, 16, 24, 26, 27, 39, 46, 47, 49
- FWHM** full width at half maximum. 23
- GWA+T** GW-approximation plus T-matrix technique. 3
- IMFP** inelastic mean free path. 3, 4
- MCP** micro-channel plate detector. 15
- MgO** Magnesium oxide. IX, X, 1, 8, 9, 19, 22, 23, 27, 28, 34, 35, 37, 38, 41
- p-eTOF** position sensitive electron time of flight spectrometer. 15, 16, 21, 47
- Pb** lead. 19
- PES** photoelectron emission spectroscopy. 48
- QMS** quadrupole mass spectrometer. 14
- S/N** signal-to-noise ratio. 5, 43, 46, 47, 51, 52
- SHG** second harmonic generation. 16
- X-op** X-ray OPTics utilities. XI, 23–25

1 Introduction

A lot of interest in the scientific community is being generated by the transport of laser excited non-equilibrium electrons. The aim of this work is to broaden the understanding of electron and hole dynamics in heterostructure systems, by using the model system Fe / Au on MgO. The Fe / Au heterostructure is often used in works studying spin resolved electron dynamics [2, 13, 28]. Despite the capability of observing transport dynamics, they were not able to analyse the interplay among relaxation and transport dynamics. Recently published works on perovskites have shown the importance of the energy resolved information when trying to understand if the propagation dynamics are ballistic or (*super*)-diffusive [37]. The novelty of this work is in using *time-resolved* linear Photoemission (*tr*-LPE), in both the established front side pump (FP) geometry to pump and probe on the Au surface, as well as the back side pump (BP) geometry analysing the non-equilibrium transport dynamics by exciting the electrons in the Fe-layer and probing them after propagation through the Au-layer at the Au surface. By varying the thicknesses of the Au-layer this work will attempt to disentangle the effects from the different constituents. This kind of information is highly interesting for applications like solar technology or spintronics.

2 Theoretical Background

2.1 Elementary Scattering Processes

The next section will cover electron scattering processes, and give an overview of the important mechanisms playing a role in the dynamics of electron transport and relaxation. After excitation the 'hot' electrons start moving away from their initial position in a random direction and separate distinct scattering processes on different timescales will dissipate the excess energy into the system. This section focuses on the dynamics that take place within the first picosecond [11].

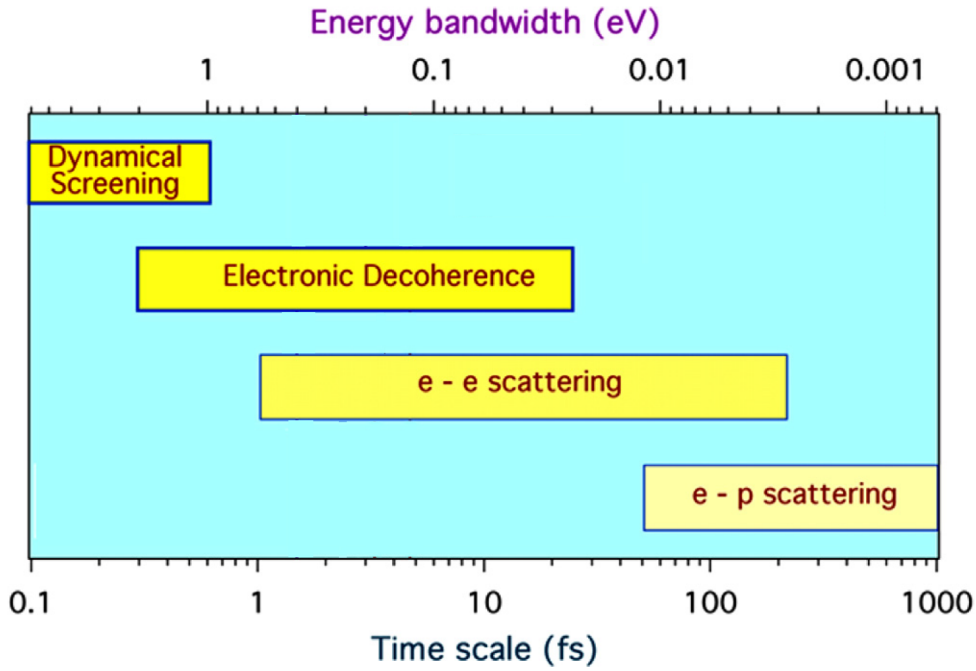


Figure 1: The characteristical timescales of electron dynamics in metals [7].

In Fig.1 the timescales of the excitation dynamics are shown. The processes correspond to the time scale at the bottom. The top axis shows the energy bandwidth as dictated by the time energy uncertainty. The used probe beam of 200 nm has a corresponding wave period of 0.66 fs. The fastest electron dynamic is the screening of the charge created by the formed hole state through nearby ground state electrons. This is the reason why direct radiative recombination of electron-hole pairs becomes very unlikely. Next, the photon-excited electrons lose phase coherence and start to scatter. These electron-electron scattering (e-e scattering) events almost exclusively occur with 'cold' electrons below or at E_F , generating new, so called, secondary electrons. Then after a few hundred femtoseconds and longer, the electrons start scattering with the lattice phonons (e-ph scattering) transferring the energy from the electronic system into the lattice. During all these processes the electrons propagate through the metal, see section 2.2 [7].



2.1.1 Electron-Electron Interactions

The first e-e interaction is the screening of the induced charges. The electrons are subject to Coulomb forces between each other, which can be seen as an average electric field that an electron experiences. If an electron gets excited into a higher state, the leftover hole gets screened by the cloud of electrons available to spread over this emerging Coulomb source [43]. This screening occurs on the order of attoseconds [11]. After the ground state electrons screen the charge of the leftover holes, the excited electrons start losing coherence. This loss of phase coherence is the main reason direct recombination with the formed hole state becomes unlikely. The excited electron loses coherence due to interaction with electrons and phonons. The biggest contributing factor here is e-e scattering with 'cold' electrons and elastic scattering with phonons [5]. The e-e scattering length is dependent on the inelastic mean free path (IMFP). GW-approximation plus T-matrix technique (GWA+T) was used in *ab initio* calculations to determine the IMFP of Fe and Au. GWA+T is an approach to calculate the self-energy in a many body system, the T-matrix adds interactions with secondary electrons and holes [42]. The calculated IMFPs lie in the order of 4 to 8 nm for spin-majority electrons in Fe, while Au with a much larger phase space near the E_F the IMFP lies around 20 to 70 nm [42, 43]. The e-e scattering can be split up into separate contributions by the different constituents of the heterostructure using an additive, Matthiessen's rule like, approach. The individual scattering channels Γ_i add up to a total scattering rate $\Gamma = \sum_i \Gamma_i$. In the studied system the decay channels are Fe Γ_{Fe} , Au Γ_{Au} and the interface $\Gamma_{Au/Fe}$ [11, 24].

2.1.2 Electron-Phonon Interactions

The influence of phonons on the total scattering rate is temperature dependent. Since at room temperature the electron-phonon scattering is *quasi*-elastic, a large momentum change can occur, but only a small portion of energy gets carried into the lattice [38]. In Copper the energy transfer by electron-phonon scattering was estimated to be about 15 meV per event [12].

2.2 Electron Transport

To understand the relaxation dynamics of electrons through e-e scattering and electron-phonon scattering (e-ph scattering) transport effects need to be considered as a part of the relaxation, too. After excitation by electromagnetic radiation the electron enters an

elevated state in which it starts moving in a random direction. If the

electron hits a barrier, like interfaces to insulators or interfaces without an overlapping wavefunction of the excited electron and the unoccupied state, it gets reflected. Otherwise the electron travels ballistically at Fermi velocity deeper into the sample [6]. Then like

in section 2.1.1 described the electron starts to scatter, this reduces the velocity of the excited electrons. Hohlfeld et al. [20] described three different time scales and velocities of electron movement, see Fig. 2 [20]. Directly after excitation by a Gaussian pump pulse the

hot electrons get injected into the conduction band of the metal. Here they now start moving in a ballistic motion away from the surface towards the bulk. Contributions by in plane transport are ignored, because the size of the focal spot of the laser is with $100\mu\text{m}$ much larger than the IMFP of the electrons [42]. During this time they move with

a velocity of about 10^6 m/s until they experience a scattering event. On the timescale of the thermal equilibrium, the electron distribution can now be characterised by the Fermi-liquid theory. Hohlfeld is now talking about hot electron diffusion, which is two orders of magnitude slower than ballistic movement due to many scattering events. During this time the electron and phonon temperature can be modelled by two-temperature model, assuming to separate heat baths for electrons and phonons which start interacting at a certain coupling constant. Until they reach thermal equilibrium, the process is dominated by thermal lattice diffusion which decreases the velocity even further to 10^2 m/s [20].

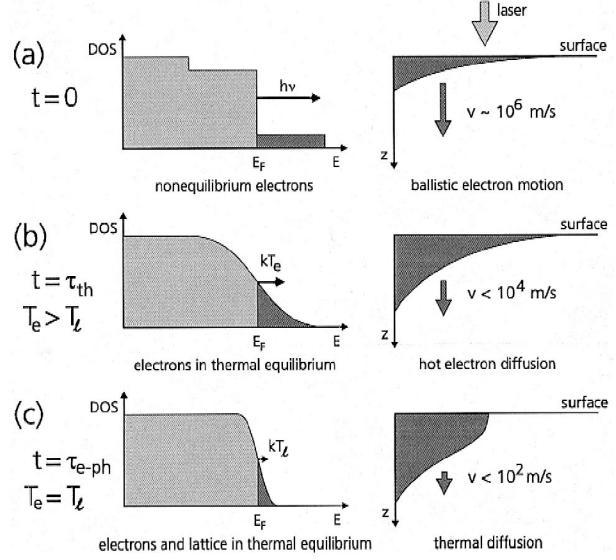


Figure 2: Depiction of the DOS against the energy of the electronic system (left) and the velocity dispersion of the hot electrons away from the surface in the z direction (right). (a) describes the non-equilibrium electrons at time zero during excitation, (b) is in the timescale of thermal equilibrium for the electrons and (c) describes thermal and lattice equilibrium [20].

Since this thesis ~~shows experiments which studies~~ dynamics before e-ph scattering takes place, ~~the~~ work of Battiato et al. [6] helped to discern more detailed aspects of the electron transport dynamics. Their work on calculating laser excited non-equilibrium electrons pointed out that there is no clear cut between ballistic and diffusive motion, but there is a so called *super*-diffusive regime in which scattering is not absent like in ballistic motion, but the scattering events are too few to label it diffusive transport [6]. ~~Considering the performed experiments are located in the described time frame of a few femtoseconds to a picosecond, this theoretic work will help, further the understanding of the results.~~ Battiato et al. [6] simulated for Fe/ Al heterostructure system, but a change to Au should just change the scattering rates, which move the curve, ~~like indicated by the dashed line in Fig. 3.~~

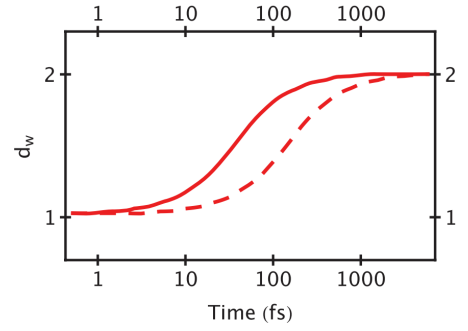


Figure 3: Anomalous diffusion coefficient for a period of time of a couple of picoseconds. Here an anomalous diffusion coefficient of one expresses a ballistic motion, while two characterises a diffusive motion [6].

2.3 Time Resolved Linear Photoemission Spectroscopy

There are two different major types of photoelectron spectroscopy, where the electrons are excited over the vacuum energy by using ultrashort laser pulses. In 2PPE and LPE one ~~use~~ two photons for excitation and probing the sample. By varying the time delay between ~~the~~ the two pulses, both techniques gain access to the temporal evolution of the non-equilibrium electron relaxation dynamics. In 2PPE the energy of each photon is lower than the workfunction Φ of the material, which needs to be exceeded to detach an electron from the material. So in 2PPE an electron only leaves the material if one photon ~~beam~~ raises the electron into an excited state and the second photon ~~again~~ excites the elevated electron to a state above the vacuum energy, see Fig.4 (left). ~~This method leads to a good signal-to-noise ratio (S/N), but it has a limited measurable unoccupied energy range and acts complementary to the used LPE.~~ By using a second photon with a lower energy than ~~the~~ the workfunction Φ in LPE, ~~we~~ achieve not only insight into the excited state, like in 2PPE, but also into occupied states through the depletion of electron population. In this work, the decreasing photoemission intensity in the depletion of electronic states below the Fermi-level E_F will be referred to as hole states.

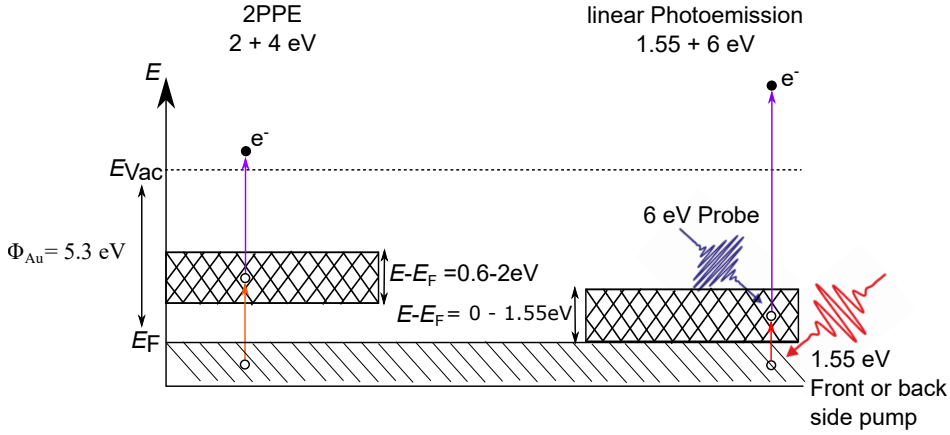


Figure 4: Depiction of the 2PPE (left) and LPE (right) excitation process for the model system using the workfunction Φ_{Au} of Au. Hatched area is the detected energy window above E_F .

The Fig. 4 depicts the difference between 2PPE and LPE on a Au surface, indicated by the workfunction $\Phi_{Au} = 5.3 \text{ eV}$, whereby the hatched areas present the probed regions of the excited states. The clear advantage of LPE is the ability to probe right up and even below the E_F . For LPE the probe photons, here a 6 eV beam, already has a photon energy higher than the workfunction of the probed material. This means the probe can access all electronic states above the E_F and part of the states below the E_F .

$$E_{\text{below } E_F} = E_{\text{Probe}} - \Phi \quad (1)$$

With Θ being the workfunction of the material and E_{Probe} the used photon energy of the probe beam, giving us the observable range below the E_F . By increasing the probe energy one can look into lower lying ground states, or by varying the pump energy gain access to a different area of the unoccupied states. Since *tr*-LPE probes below the E_F , the excitation by the pump beam even reveals hole states and their dynamics.

2.4 Optical Penetration Depth

One important factor for the study of electron dynamics is the excitation mechanism. The depth of excitation is given by the optical penetration depth λ_{OPD} . The λ_{OPD} is a measure of how deep an electromagnetic wave can access a material. When observing electron dynamics and trying to understand electronic proliferation and transport in a material it is important to understand where the probe beam is actually exciting electrons over the vacuum level to be probed. The transport of the electronic excitation is partly determined by the mean free path of the excited electrons and holes. The here used definition is, when the intensity of the light falls to $I = 1/e \cdot I_0$, so about 36,8 % [40]. In this work two approaches were used to estimate the λ_{OPD} :

- The λ_{OPD} was calculated via the absorption coefficient, with the λ_{OPD} correlating to $1/\alpha$ to get a rough estimate. To calculate the absorption coefficient and thus the penetration depth the following equation was used [34].

$$\frac{1}{\alpha} = \frac{\lambda_0}{4 \cdot \pi \cdot \kappa} \quad (2)$$

with λ_0 being the vacuum wavelength of the incident light and κ the extinction coefficient. The extinction coefficient was taken from Weaver and Krafka and is plotted in Fig.12 in section 2.6.2 for Fe and Fig.8 in section 2.6.1 for gold [21]. This gave the following values for the different materials and wavelengths of light.

Table 1: Optical penetration depth λ_{OPD} for the different constituents and wavelengths.

Wavelength [nm]	Fe [nm]	Au [nm]
200	11.3	13.96
800	16.89	12.78

This approach gives a good approximation, which coincides with the results for Au for laser profile calculations, see section 4.1. But it does not consider the scattering processes at the Fe-Au interface and assumes bulk properties. In thin film systems, which are smaller than the estimated thicknesses this leads

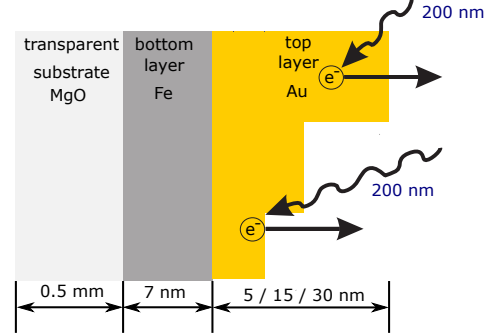


Figure 5: Illustration of optical penetration for thin film samples, in front side pump [25].

to considerable errors, because interface contributions play a major part in light propagation.

- The second approach calculates the field intensity directly by using the dynamical theory of diffraction and takes into account multiple scattering events. This theory was originally developed to calculate the interaction of a wave with a periodic lattice. Typical uses for this theory is the calculation of Bragg and Laue peaks for X-ray diffraction. These calculations were performed in this work and are discussed in section 4.1.

2.5 Hole Dynamics

A hole is the absence of an electron in the valence band. In every two photon photoemission spectroscopy holes are created by the pump beam, but in most cases the excited non-equilibrium electrons are of interest and the created holes do not get observed. Holes are less mobile than electrons and have a lower velocity, because they move by electrons filling the vacant spot in the valence band. Because of the screening of the positive charge of holes and the high number of electrons in the valence band, holes are difficult to be observed.

2.6 Au/Fe/MgO(001) Heterostructure System & Electronic Bandstructure

As a model system to study the effects of electron transport, an Fe-Au heterostructure on MgO was chosen. The MgO substrate provides a (001)-crystal surface, which is ideal for epitaxial growth and, thus, important for sharp crystalline interfaces. This enables to neglect interface scattering contributions in the analysis of electron relaxation dynamics. Furthermore MgO has good transmittance for the 800 nm pump-beam, because of the 7.8 eV band gap [31]. The dimensions of the MgO crystal are 10 mm by 10 mm with a thickness of ± 0.02 mm. The first layer on the MgO is a 7 nm thick, epitaxially grown Fe film and on top of this a second epitaxially grown layer of gold with varying thicknesses. The Fe layer, due to its good absorption in the visible range, acts in back side pump configuration as an injection layer of hot electrons into the Au-layer. Those excited electrons propagate through the Fe-Au interface towards the Au-layer surface

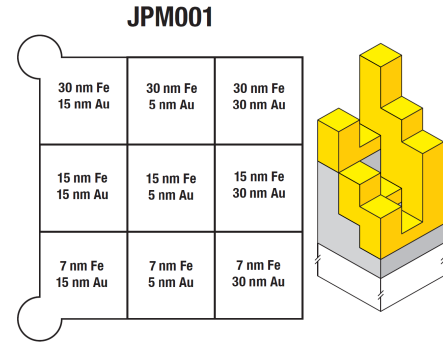


Figure 6: Layout of the sample film thicknesses (left) and three-dimensional visualisation (right). The lateral dimensions of the sample are 9 mm by 9 mm.

and will be then probed out of the sample by a time delayed UV pulse with the photon energy $E_{probe} = 4 \text{ eV}$. Laser absorption profiles will later show that most of the energy of the pump beam, in case of back side pump configuration, is absorbed in the Fe-layer. In case of front side excitation, the pump beam excited directly on the probed surface and the influence of Fe as a trap for the electrons by changing the thickness of the Au-layer can be observed. The utilised sample was grown by D. Diesing and J.P. Meyburg of the physical chemistry department in the university Duisburg-Essen using molecular beam epitaxy (MBE). The sample layout is shown in Fig. 6. The substrate is a 9 mm x 9 mm square of a 0.5 mm thick MgO on which nine different 3 mm x 3 mm areas of Fe/ Au layers are grown in a $[001]_{\text{Au}} || [001]_{\text{Fe}} || [001]_{\text{MgO}}$ orientation. The epitaxial growth of the different layers and their pristine interface are shown by Mühge et al. for MgO/ Fe [29] and Dekadjevi et al. for Fe/ Au [17]. The layers are grown in three rows of separate iron thicknesses (7 nm, 15 nm and 30 nm) and three columns of gold thicknesses (5 nm, 15 nm and 30 nm). Since previous experiments have shown that increasing the Fe thickness only reduces injection efficiency of hot electrons, see supplement of Beyazit et al. [9], only the 7 nm Fe row of the sample was used. For understanding the dynamics that are being observed, it is important to know the bandstructure of Au and Fe.

2.6.1 ~~Chemical~~ Properties of Gold

Hammer and Nørskov identified, that "the unique role that gold plays in society is to a large extent related to the fact that it is the most noble of all metals" [30]. Gold is a noble metal, with a full 5d-band and a half filled 6s-band, that governs the chemical and optoelectronical behaviour of gold.

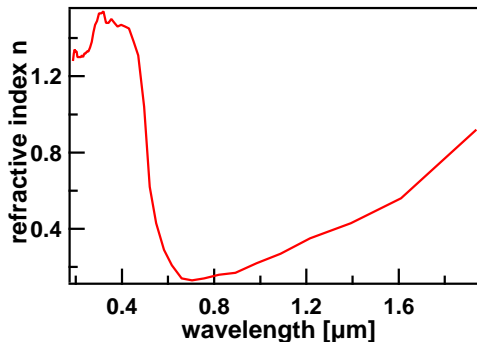


Figure 7: The refractive index n of gold from 200 to 2000 nm. Taken out of the optical handbook from Palik [32].

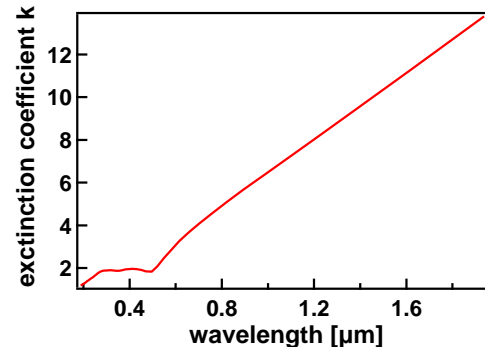


Figure 8: The extinction coefficient κ of gold from 200 to 2000 nm. Taken out of the optical handbook from Palik [32].

The two graphs show the real and imaginary part of the complex refractive index, as

shown in eq. 3.

$$\tilde{n} = n + ik \quad (3)$$

The real part n , the refractive index, of the complex refractive index \tilde{n} describes the phase velocity of the wave in the medium it is travelling in, while the complex part k , the extinction coefficient, represents the attenuation of the wave in the medium. The refractive index in Fig. 7 shows, a minimum at the used wavelength of 800 nm, when using front side pump, while the attenuation is quite higher, than for the 200 nm probe beam. The bandstructure of gold and the density of states (DOS) gives knowledge about what electrons participate in the excitation process and what states are being filled. These band structures show the energy dispersion of the electronic bands for different directions on the Brillouin zone. The s and p orbitals are characterised by broad band dispersion, because they are not strongly localised in the electronic structure. Whereas d orbitals are tightly bond to the core and exhibit a very small band with a high density of states [19]. The bandstructure of gold, see Fig. 9, shows that there are very few bands around the E_F , those bands have a s,p character. This is reflected by the low DOS around E_F until about 1.5 eV below E_F , see Fig. 10. The sharp rise in the DOS is attributed to the d-bands, see Fig. 9, located about 2 eV below E_F [8]. Since gold has a full d-band, that is also lower in energy compared to the lighter counterparts of the noble metals, the d-band density of states is very narrow [30].

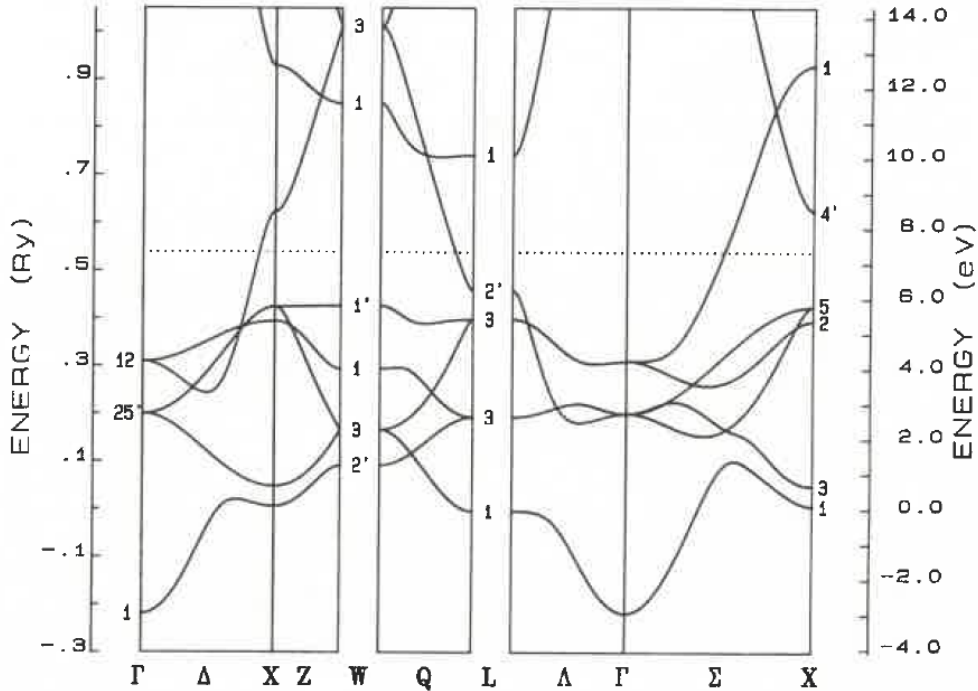


Figure 9: Calculated band structure of gold, the dashed line corresponds to the Fermi-level. Taken from Papaconstantopoulos [33].

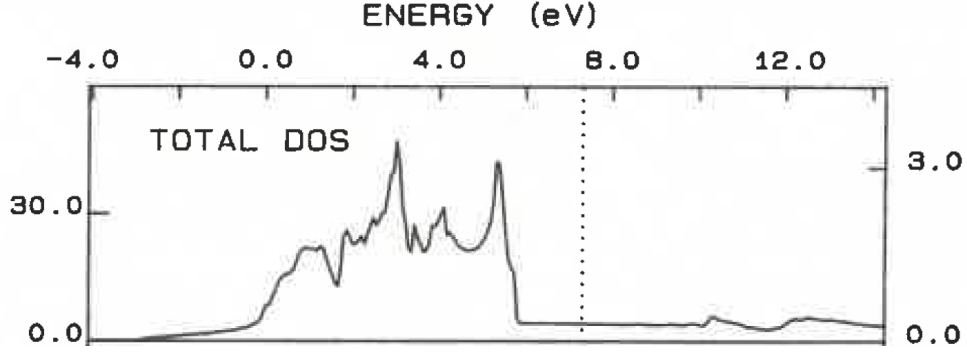


Figure 10: The density of states of gold taken from Papaconstantopoulos [33]. The dashed line depicts the Fermi-level.

[19]

2.6.2 ~~Chemical~~ Properties of Iron

Iron is a ferromagnetic ~~3-d~~ transition metal. It crystallises in a body-centered cubic (bcc) unit cell and has a lattice constant of 286.6 pm. This is important for gold to be able to grow epitaxially on the iron lattice in the $[001]_{\text{Au}} || [001]_{\text{Fe}} || [001]_{\text{MgO}}$ as shortly elaborated in section 2.6.1.

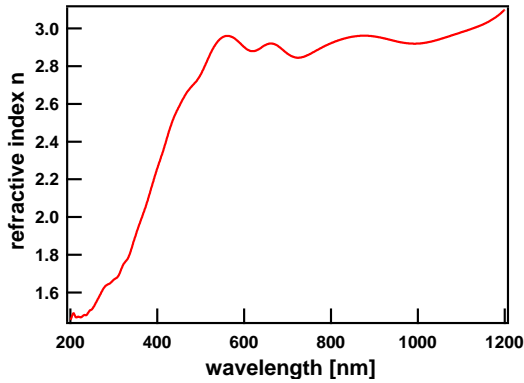


Figure 11: The refractive index n of iron from 200 to 2000 nm. Taken from Johnsen and Christy [22].

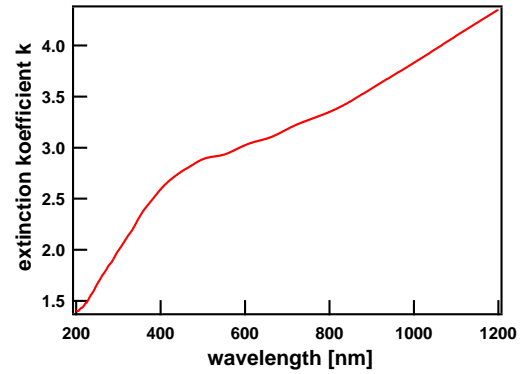


Figure 12: The extinction coefficient κ of iron from 200 to 2000 nm. Taken from Johnsen and Christy [22].

The plotted graphs show the real and imaginary part of the complex refractive index for Fe. The refractive index is quite constantly high above 500 nm in Fe. The plotted extinction coefficient κ in Fig. 12 correlates, as shown in eq. 2, to the absorption of iron, which is dependent on the wavelength of the incident light. The graph shows a steady increase in the extinction coefficient with rising wavelength. The plot shows, that the 800 nm beam is strongly absorbed by the injection layer iron in the back side pump / front side probe experimental configuration. The DOS of iron shows a lot of

majority spin electrons below and around the Fermi-level, while the minority spins are shifted up by about 2 eV.

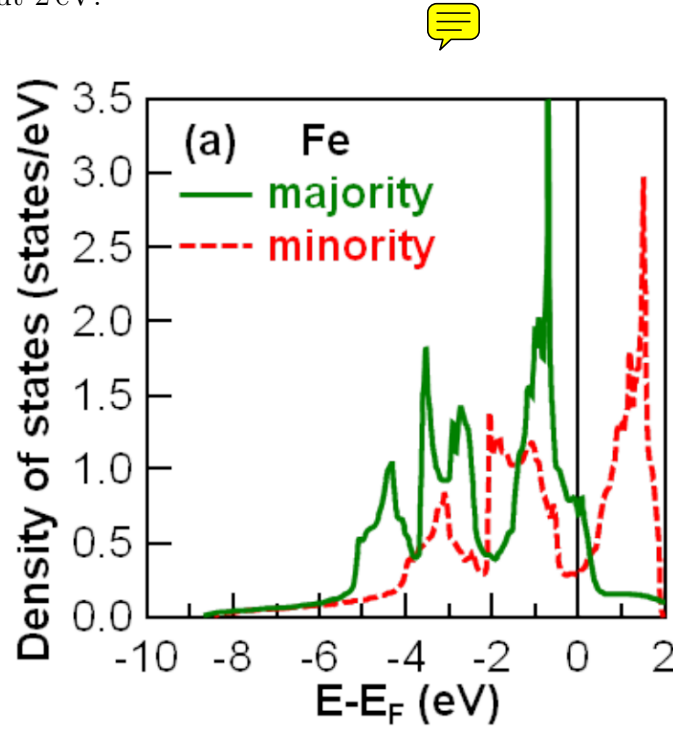


Figure 13: Density of states of bcc-iron split into majority (spin up) and minority (spin down) electrons. Taken from Alekhin [1].

Momentum averaged transmittance calculations done by Alekhin in his PhD thesis showed that almost exclusively majority electrons get transmitted across the Fe-Au interface [1]. This means that in this experiment mostly majority electrons are contributing to the signal reaching the Au-surface.

Eigenständigkeitserklärung

Hiermit erkläre ich, dass ich diese Arbeit selbstständig verfasst, keine anderen als die angegebenen Quellen und Hilfsmittel benutzt, sowie Zitate kenntlich gemacht habe.

Duisburg, 21.08.2020

Florian Kühne